

On the Cooling Rate-Microstructure Relationship in Molten Metal Gas Atomization



DARIO GIANOGLIO, NEVAF CIFTCI, SARAH ARMSTRONG, VOLKER UHLENWINKEL, and LIVIO BATTEZZATI

Gas atomization is the most used powder production technique since it provides good control on particles shape, surface oxidation and dimension. It is a rapid solidification technique involving fast cooling rates, which are strictly correlated to particle size. This relationship is typically described with a power law function that can be determined experimentally by measuring the microstructural length-scale or through the application of a heat transfer model. Both paths were exploited in the present work focusing on a gas-atomized Al-4.5Cu alloy. Atomized powders were characterized by means of X-ray diffraction, differential scanning calorimetry, light and scanning electron microscopy to investigate the relationship between cooling rate and microstructure length-scale. A recently proposed semi-empirical model was validated and discussed in terms of a physically based heat transfer approach. The change in gas-to-melt mass flow ratio (GMR) was also investigated showing that it does not affect appreciably the relationship between solidification rate and particle size, but does increase the Cu supersaturation in the powders of finer size.

<https://doi.org/10.1007/s11661-021-06325-2>
© The Author(s) 2021

I. INTRODUCTION

POWDER metallurgy provides feedstock material for processes such as Metal Injection Moulding, Hot Isostatic Pressing, Cold Spray Deposition as well as for cladding, welding and coating purposes. The interest in powder production has further increased with the advent of Additive Manufacturing (AM) processes as strictly controlled powder size distribution (PSD) is required to obtain dense products. For techniques such as Laser Powder Bed Fusion (LPBF), a wide PSD will affect the powder flowability causing inhomogeneity of the powder layer. This results in high porosity or unmelted regions in the final object with serious impact on its mechanical properties.

Gas atomization (GA) is the most used powder production technique for AM purposes because it gives spherical particles with tailorable PSD and limited surface oxidation. The cooling rate (CR) in the temperature range of solidification is typically linked to the

particle size (d_p). In case of unsteady-state heat flow solidification, the dependence is commonly expressed by a power law function:

$$CR = a_0 \cdot d_p^{a_1} \quad [1]$$

in which d_p is the particle diameter, a_0 and a_1 are two alloy-dependent parameters that can be determined experimentally or by means of thermal heat transfer models.^[1–3]

Microstructural features in solidification,^[4–7] segregation events^[8–10] and the atomization process^[11,12] have been studied and simulated. The microstructural length-scale is conventionally measured and correlated to the cooling rate afterwards as it is difficult to directly measure cooling rates during melt atomization experiments. A semi-empirical correlation based on the characterization of the microstructural features of a Cu-Sn alloy has been recently proposed to express the parameters in Eq. [1].^[13] In the present work, the correlation is checked for gas-atomized Al-4.5Cu. The Al-Cu system has been chosen because of the availability of previous studies on atomization and solidification.

In conventional castings following the equilibrium phase diagram,^[14–16] Al-Cu alloys solidify with primary dendritic structures, then Cu segregates in the interdendritic zones where the Al- θ -phase eutectic is formed.^[17–19] The microstructure depends on the cooling rate^[20] affecting grain size as well as primary and secondary dendrite arm spacings of primary Al (λ_1 , λ_2). For a given alloy composition processed through any

DARIO GIANOGLIO and LIVIO BATTEZZATI are with the Dipartimento di Chimica, Università di Torino, Via Pietro Giuria 7, 10125, Torino, Italy. Contact e-mail: dario.gianoglio@unito.it. NEVAF CIFTCI is with the Leibniz Institute for Materials Engineering IWT, Badgasteiner Straße 3, 28359 Bremen, Germany. SARAH ARMSTRONG and VOLKER UHLENWINKEL are with the Leibniz Institute for Materials Engineering IWT and also with the University of Bremen, Faculty of Production Engineering, Badgasteiner Straße 1, 28359 Bremen, Germany.

Manuscript submitted October 19, 2020; accepted January 5, 2021.

Article published online June 23, 2021

rapid solidification technique, all of these features become finer the faster the cooling rate.^[21] The increase in cooling rate determines the transition from dendritic to cellular growth of the primary phase up to a critical solidification front velocity above which solute segregation is hindered and solidification occurs as single-phase planar front.^[22] Such an event is extremely rare in gas-atomized powders and was observed in Al-6wt pct Si particles of sub-micrometric size but not in Al-Cu ones.^[23] Serreal *et al.*^[24] reported the discrete distribution of the θ -phase around primary dendrites in an Al-4.9Cu alloy produced by melt spinning where the cooling rate was estimated to be 1700 K/s. Liu *et al.*^[25] found a cellular microstructure in gas-atomized Al-alloys powder, with the Cu content varying from 1 to 5 wt pct and the particle size ranging from 10 to 40 μm . The cell and grain sizes were comparable although some small cells showed low-angle grain boundaries in a single grain. Cu segregated at grain boundaries and the eutectic network appeared more continuous the higher the Cu content in the alloy. The increase in Cu content leads to finer dendrites and to microstructure refinement.^[26,27] Bedel *et al.*^[28] studied impulse-atomized Al-4.5Cu particles focusing on particles sizes smaller than 300 μm . They identified four solidification morphologies in similar droplets belonging to the same powder batch, which were apparently subjected to a range of solidification velocities. They reported that the cooling rate is strictly correlated to the droplet diameter, and it has a small influence on the solidification morphology allowing the coexistence of cellular and dendritic features independently from the microstructural length-scale. The probability of multiple nucleation events was estimated to be lower than 5 pct. This result was confirmed by a statistical analysis carried out by Valloton *et al.*^[29] The probability of having multiple heterogeneous nucleation sites is low for small droplets and increases as the particle size increases with two consequences: multiple nucleation events are more probable in large particles and nucleation occurs at different undercooling levels as a function of the droplet size. Solute trapping can take place in small particles.^[30] Recalescence contributes to the particle temperature increase and the cooling rate decreases with increasing particle size. A transition in the solidification microstructure from planar to cellular to dendritic occurs.^[31] Despite the presence of different microstructures, Prasad *et al.*^[32] proved that the microstructural length-scale can be considered constant in each particle. Therefore, for solidification at steady-state heat flow, the average λ value that depends on the cooling rate is given by^[33]:

$$\lambda = a \cdot \text{CR}^b \quad [2]$$

The present study is aimed to characterize gas-atomized Al-4.5Cu powders as well as to investigate the efficiency of the semi-empirical model proposed by Ciftci *et al.*^[13] which predicts the cooling rate in molten metal gas atomization. Results are compared with literature and a heat transfer model is used to get insight into the

role of convection, conduction and radiative dissipation when atomizing Al alloys. The effect of the gas-to-melt mass flow ratio (GMR) on cooling rate is also studied.

II. MODELLING BACKGROUND

This work is aimed at verifying a predictive route for the determination of the pre-exponential parameter a_0 in Eq. [1]. The model was presented in detail earlier.^[13] It has mainly an applicative approach aiming at correlating the behaviour of different alloys and atomization plants. It compares average cooling rates derived from Eq. [1] and calculated average cooling rate derived from the secondary dendrite arm spacing method (SDAS). It also allows the investigation of critical process parameters such as gas-to-melt mass flow ratio and the initial gas temperature. The model is based on thermophysical properties of the melt to obtain the overall heat released by the droplets in the temperature interval of solidification according to the equilibrium phase diagram and considers the surrounding gas cooling power in terms of the difference between the alloy average temperature and the gas temperature. The alloy average temperature is assumed to be the temperature at solid fraction $f_s = 0.5$. The a_0 parameter is obtained according to the following equation:

$$\frac{a_{0x}}{a_{0ref}} = \frac{\rho_f \cdot (c_{pLx} [T_{Lx} - T_{Sx}] + \Delta h_x) \cdot (T_{Lx} - T_{Sx}) \cdot \left(\frac{T_{Lx} + T_{Sx}}{2} - T_g\right)^{-1}}{\rho_{fref} \cdot (c_{pLref} [T_{Lref} - T_{Sref}] + \Delta h_{ref}) \cdot (T_{Lref} - T_{Sref}) \cdot \left(\frac{T_{Lref} + T_{Sref}}{2} - T_g\right)^{-1}} \quad [3]$$

where ρ_f is the density of the melt droplet at solid fraction of 0.5, c_{pL} is the specific heat capacity of the liquid melt droplet, Δh is the latent heat of fusion. T_L , T_S and T_g are the liquidus, solidus and gas temperature, respectively. Subscript “x” refers to thermophysical quantities of the alloy under investigation (Al-4.5Cu in the present work), which are related to the corresponding parameters of a reference system, identified by the subscript “ref”, i.e. the Cu-6Sn alloy gas atomized in argon atmosphere of Reference [13]. This model is independent of the atomization equipment used and it can be in principle applied to different alloys since it only requires basic physical quantities of a reference system which may be available from literature databases. Its efficiency was proven using the data of Mullis *et al.*^[1] with promising results and will be further verified in this work.

III. EXPERIMENTAL

The atomization plant was equipped with 2 litres graphite crucible and a stopper rod that controls the melt flow through the nozzle. Al-4.5Cu powders were gas-atomized after melting pure Aluminum (99.999 pct) and an Al₅₀Cu₅₀ pre-alloy (KBM AFFILIPS) at 1271 K with a melt superheat temperature of 350 K. The temperature was kept constant for 20 minutes to homogenize the liquid. Nitrogen was

used as atomization gas but also to control the atmosphere in the atomization plant. The oxygen content was below 0.5 ppm at the top of the plant and increased up to values of few thousands ppm in the cyclone (particle separator) after solidification by purging from the bottom of the plant a mixture of gas composed by nitrogen + 3 vol. pct oxygen whilst atomization occurred. This was necessary to control surface passivation since explosion issues may occur in aluminium powders. During atomization experiments the pressure above the melt is increased automatically to compensate the volume difference in the crucible and to ensure a steady state flow condition of the melt. The atomization pressure was set to 1 MPa leading to a gas mass flow of 0.11 kg/s. A close-coupled atomizer was used with a 0.8 mm annular slit (CD-CCA-0.8).^[34] Different nozzle diameters (1.5, 2, and 3 mm) were used resulting in different GMR values ranging from 2.4 ± 0.2 to 7.2 ± 0.2 . The powders were air-sieved with 25, 45, 63, 90, 125, 150, 180, 200, and 250 μm sieves into corresponding particle class sizes. The particles were then embedded in cold mounting resin, ground and polished with a 1 μm diamond suspension. The microstructure was revealed by etching in a NaOH and distilled water solution (1:9 in weight) for 15 s. The cells spacing (λ) was measured with an Olympus BX51 optical microscope equipped with an Olympus DP27 high-resolution camera. A SUPRA 40 (Zeiss) scanning electron microscope equipped with a backscattered electron detector was used to measure cells spacing on unetched particles smaller than 25 μm . Ten particles were analysed for each size fraction and five cells spacing measurements were performed on every particle using the linear intercept method^[35]:

$$\lambda = \frac{L}{n-1} \quad [4]$$

where L is the length of the line drawn on the micrograph crossing (n-1) cells and n is the number of cell borders encountered. The λ average value is calculated from 50 measurements for each particle size fraction. Data were collected from particles having cross-section diameter in the range of the corresponding size fraction to avoid contributions from bigger or smaller particles which are not eliminated by sieving. For the rest of this work, we will refer to the mean particle cross-section diameter to indicate particle sizes.

Phase identification and supersaturation levels were determined by means of XRD analysis carried out with a PANalytical X'Pert PRO diffractometer by Philips equipped with an X'Celerator detector and Cu anode whose $K\alpha$ radiation is 1,5418 Å. The investigated 2θ angle range was 20-140° in continuous scan mode with a step size of 0.0167°. Rietveld refinement was carried out employing the Maud programme.^[36]

Calorimetric analyses were performed with a DSC TA Q100 device in the temperature range from 232 K to 773 K with a heating rate of 20 K/min.

IV. RESULTS AND DISCUSSION

A. Microstructure

Figure 1 shows the microstructure variability amongst particles of similar size (a, b), and the change in microstructure length-scale depending on particle size (c). The microstructure of the particles consists of cellular primary Al and eutectic at its boundaries. XRD analysis confirms the presence of fcc Al and tetragonal Al_2Cu (Θ -phase). Because of Cu supersaturation in solid solution, less Cu is available to form the eutectic. Therefore, the eutectic network is often interrupted. A dendritic microstructure was also observed in a few particles. The eutectic continuity at grain boundaries and dendrite formation seems to be independent of particle size which is in agreement with previous findings.^[28]

B. Cooling Rate – Particle Diameter Correlation

After measuring the cell spacing as a function of the particle size as previously described, the cooling rate was calculated for each λ value using the following correlation obtained by Mullis *et al.* which is based on several experiments performed on Al-Cu alloys in the last 50 years^[1]:

$$\lambda = 58.7 \cdot CR^{-0.355} \quad [5]$$

The correlation proposed by Mullis *et al.* was considered as a reliable reference to evaluate the quality of our data and of the models proposed in this work. Figure 2(a) shows the calculated cooling rate as a function of the droplet diameter. The experimental data in this work is compared with the results of the semi-empirical model (Eq. [1]), and with a model presented by Mullis *et al.* based on SDAS analysis for the particle size considered in each work. An average cooling rate is considered for the entire solidification time interval.

The semi-empirical model by Ciftci *et al.*^[13] focuses on a_0 determination whilst a_1 was imposed equal to -1.67. Despite the a_1 value obtained from the linear fit of experimental points being higher in absolute value, the empirical correlation is in good agreement with the results of Mullis *et al.*^[1] The exponential and pre-exponential parameters for Eq. [1] are reported in Table I.

C. Insights from a Heat Transfer Model

The correlation between cooling rate and particle size was studied by several authors through the years making use of the well-established heat transfer theory.^[29,37–39] The correlation can be achieved by means of a model based on the heat balance equation,^[40] considering the heat removed by conduction, convection and radiation including the latent heat of solidification. The model describes the solidification rate of a spherical droplet during gas atomization cooled in Newtonian condition assuming negligible evaporation from the surface of the particle and homogeneous nucleation according to the

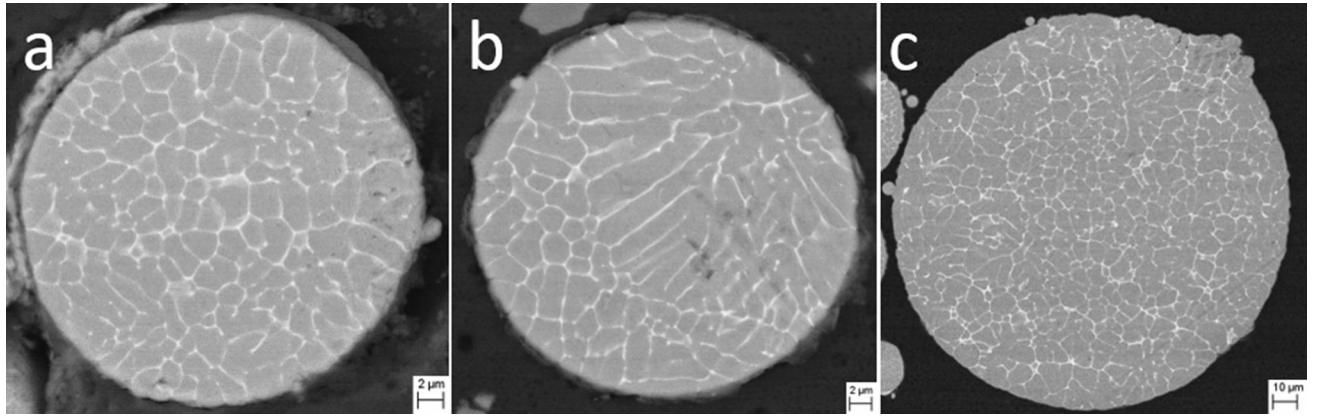


Fig. 1—Microstructure of gas-atomized Al-4.5Cu particles belonging to different particle size classes: (a, b) 25-45 μm ; (c) 180-200 μm .

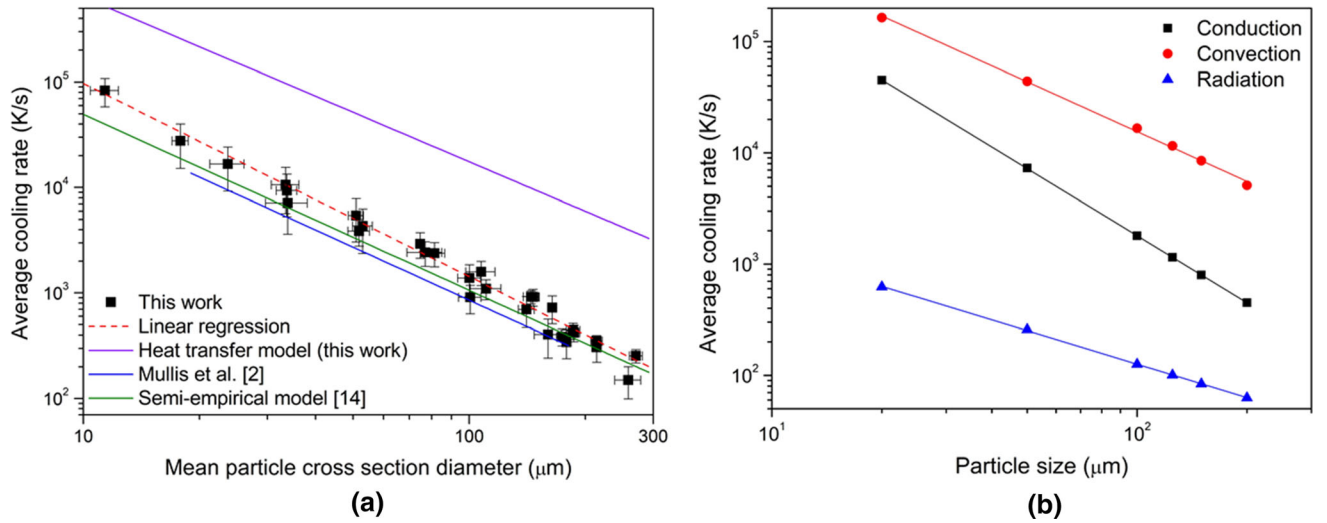


Fig. 2—(a) Average cooling rate for Al-4.5Cu gas-atomized powders calculated in the solidification time interval as a function of the mean particle cross section diameter; (b) conductive, convective and radiative contributions to the overall average cooling rate obtained from the heat transfer model.

classical nucleation theory. The cooling rate can be expressed according to^[29]:

$$\frac{dT}{dt} = \frac{-6[h_{eff}(T_p - T_g) + \varepsilon\sigma(T_p^4 - T_w^4)]}{\rho_p d_p c_{s,p}} \quad [6]$$

where ρ_p , d_p and $c_{s,p}$ are the droplet density, diameter and specific heat, respectively. h_{eff} is the effective heat transfer coefficient, ε is the droplet emissivity and σ is the Stefan-Boltzmann constant whilst T_p , T_g , and T_w are the particle, gas and wall temperatures. The temperature across each particle is supposed to be instantaneously homogeneous and the wall temperature is fixed at 300 K. The temperature of the gas is calculated as a function of the position with respect to the particle motion according to the relationship proposed by Grant *et al.*^[40] The specific heat in the temperature interval where solidification occurs accounts also for the latent heat of fusion (ΔH_f) according to:

$$c_{s,p} = \frac{\Delta H_f}{T_L - T_S} + \frac{c_{s,l} + c_{s,s}}{2} \quad [7]$$

in which T_L is the liquidus temperature, T_S is the solidus temperature, $c_{s,l}$ and $c_{s,s}$ are the specific heat in the liquid and solid-state, respectively. The alloy physical properties used for the simulation are listed in Table II.

In order to highlight the effect of droplet diameter in different processes, it is useful to develop the effective heat transfer coefficient which is defined as a function of Reynolds number (Re) and Prandtl number (Pr) as follows:

$$h_{eff} = \frac{k_g(2 + 0.6\sqrt{Re}^3\sqrt{Pr})}{d_p} \quad [8]$$

$$Re = \frac{v\rho_g d_p}{\mu_g} \quad [9]$$

Table I. a_0 and a_1 Values Relative to Eq. [1]

	a_0	a_1
This work	$2.96(\pm 0.12) \times 10^6$	$-1.67(\pm 0.08)$
Heat Transfer Model (This Work)	$2.310(\pm 0.015) \times 10^7$	$-1.59(\pm 0.02)$
Mullis <i>et al.</i> [1]	$1.87(-) \times 10^6$	$-1.67(-)$
Semi-empirical Model [13]	$2.32(-) \times 10^6$	$-1.67(-)$

Table II. Physical Properties of the Al-4.5Cu Alloy

Quantity	Value	References
ρ_p	$2605 \frac{kg}{m^3}$	Plotkowski <i>et al.</i> [41]
$c_{s,L}$	$910 \frac{J}{kgK}$	Mullis <i>et al.</i> [1]
$c_{s,S}$	$1178 \frac{J}{kgK}$	Mullis <i>et al.</i> [1]
ΔH_f	$381900 \frac{J}{kg}$	Quaresma <i>et al.</i> [19]
$c_{s,p}$	$6069 \frac{J}{kgK}$	Calculated from [1,19]
T_L	921 K	TCS Al-based Alloy 2020b [42]
T_S	845 K	TCS Al-based Alloy 2020b [42]
T_E	821 K	TCS Al-based Alloy 2020b [42]

$$Pr = \frac{c_{s,g}\mu_g}{k_g} \quad [10]$$

where k_g , $c_{s,g}$, ρ_g and μ_g are the gas thermal conductivity, specific heat, density and the dynamic viscosity, respectively, whilst v is the difference between the particle and gas velocity in absolute values. Eq. [6] can now be expressed as a function of the droplet diameter according to:

$$\begin{aligned} \frac{dT}{dt} &= - \frac{12k_g(T_p - T_g)}{\rho_p c_{s,p}} d_p^{-2} \\ &\quad - \frac{3.6k_g(T_p - T_g) \sqrt{\frac{\nu \rho_g}{\mu_g}} \sqrt{\frac{c_{s,g}\mu_g}{k_g}}}{\rho_p c_{s,p}} d_p^{-\frac{3}{2}} \\ &\quad - \frac{6\epsilon\sigma(T_p^4 - T_w^4)}{\rho_p c_{s,p}} d_p^{-1} \\ &= cr_{cond}(T) + cr_{conv}(T) + cr_{rad}(T) \end{aligned} \quad [11]$$

where the terms with different exponents of d can be referred to conduction, convection and radiation processes, respectively. The thermophysical and processing parameters to be inserted into Eq. [11] which are assumed constant are listed in Table II. Physical properties of the Al-4.5Cu alloy. The quantities depending from the temperature, such as the relative velocity, the gas dynamic viscosity and the gas thermal conductivity, are calculated together as a function of the position of the particle with respect to the point where atomization takes place. A maximum value of emissivity ($\epsilon = 1$) was considered for this work.

The average cooling rate is calculated for each contribution as a function of the particle size according to

$$CR_i = \frac{\int_{f_s=0}^{f_s=1} cr_i(T) dt}{t_s - t_l} \quad [12]$$

where the integral is calculated in the solidification interval from the moment the first crystalline stable nucleus is formed ($f_s = 0$), to the complete droplet solidification ($f_s = 1$) and i refers to each contribution once at the time. The overall average cooling rate is calculated by considering the conductive, convective and radiative contributions at the same time and plotted in Figure 2(a) whilst a direct comparison of these is reported in Figure 2(b) as described in Eq. [11] to compare the mutual effect on the overall average cooling rate experienced by the particles. The radiative contribution plays a minor role across all the range of particle size considered and it is negligible without introducing consistent errors in the CR correlation. Convection is the main mechanism responsible for the final CR, whilst conduction gains importance as the particle size decreases. The convective contributions for the case studied is three times higher than the conductive one for 20 μm particles, but it reaches a factor of 10 for 200 μm particles. From Eq. [11] it becomes apparent that the contributions to the particles cooling rate depend on the alloy in terms of density, specific heat, emissivity and melting temperature. Nonetheless, convection, conduction and radiation vary with the gas properties for a fixed alloy composition. The main parameters in this case are the thermal conductivity of the gas and the Reynolds number. The hierarchy of the CR contributions is thus defined by the experimental conditions and can change accordingly, e. g. for other alloys. Overall, the heat transfer model provides overestimated results for the cooling rate because of the approximations inherent in Eq.[8] and in the parameters taken as constant. Also, it predicts a lower a_1 parameter with respect to the empirical and Mullis' ones. This is due to an overestimated Reynolds number giving more importance to the convective factor and to the absence of particles interactions. The model considers just one particle solidifying at a time in absence of other particles which otherwise would contribute a local temperature increase resulting in a lower cooling rate. However, it highlights the relevance of the convection, conduction and radiation contributions to heat subtraction and suggests further advances in terms of modelling.

D. Effect of the Gas-To-Melt Mass Flow Rate

1. Cooling rate

The GMR is expected to affect particles cooling rate during solidification. The larger the amount of gas flowing and interacting with the molten droplets, the higher the heat flux from the surface of the particles should be. A higher cooling rate should correspond to finer microstructure.

The GMR was varied using different nozzle diameters. A nozzle diameter reduction leads to an increase in GMR. In the previous work,^[13] the following power law relationship between cooling rate, droplet diameter and GMR was proposed:

$$CR = b_0 \cdot d_p^{b_1} \cdot GMR^{b_2} \quad [13]$$

Equation [13] is used to fit the experimental data obtaining $b_0 = (6.2 \pm 0.2) \cdot 10^6$, $b_1 = -1.86 \pm 0.07$ and $b_2 = 0.08 \pm 0.11$. The pre-exponential factor and the particle diameter exponent are very similar to those presented by Ciftci *et al.*^[13] On the other hand, the value of b_2 is close to zero and carries high relative error. This suggests that the cooling rate of gas-atomized Al-4.5Cu is not affected by the relative amount of atomization gas interacting with solidifying droplets. This behaviour is probably linked to the negligible radiative heat transfer coefficient for Al alloys with respect to the convective one.^[43] For alloys having higher melting temperature, such as Fe based alloys, the radiative contribution may gain importance by decreasing the cooling rate as GMR decreases.

2. Copper supersaturation

Cu supersaturation in the primary Al phase was investigated by means of DSC and XRD analyses. Figure 3 shows two successive DSC traces for the extremes of the size classes with free cooling in between. The second scan is helpful to recognize reversible and

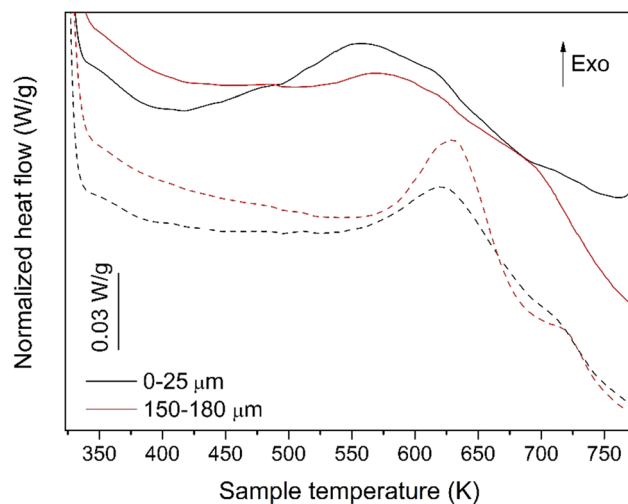


Fig. 3—DSC analysis of Al-4.5Cu powders with a particle size class of $< 25 \mu\text{m}$ and $150\text{-}180 \mu\text{m}$, respectively. The dashed lines represent the corresponding second heating ramps.

irreversible transformations in the sample and to properly attribute each signal to the corresponding phenomenon occurring in the material. The first heating ramp shows a wide exothermic signal from 500 K to 630 K and an endothermic contribution above 700 K in both cases. The exotherm is apparently composed of overlapped signals: the first maximum is higher for the smallest particles. This thermal effect is attributed to θ' precipitation from the supersaturated solid solution. It is followed by the signal due to the formation of the equilibrium θ phase occurring in a wide temperature range because of the powder variability. Fatmi *et al.*^[44] have also observed a single exothermic peak which was attributed to the formation of both θ' and θ phases. The endothermic signal at high temperature is due to the θ -phase dissolution once the temperature exceeds the solvus line. Metastable phases were fully precipitated during free cooling. The second DSC trace is characterized by an exothermic peak and a final endothermic one confirming the sequential precipitation and dissolution of the θ -phase as reported for Al-Cu alloys.^[32-34]

Nevertheless, significant broadening of fcc-Al reflections is detected in the XRD patterns. The reasons for peak broadening are fine crystals and solute trapping produced by rapid solidification. This is shown by the Al lattice parameter lowering. A gradient in Cu content is expected across each Aluminium cell^[25] which is an additional cause for peak broadening. However, Rietveld refinement was performed simplifying the system with two Al phases: the major one is closer to the overall peak shape and generally defines the position of the reflections whilst the second one mostly accounts for the background enhancement. Figure 4 reports the (420) reflections and the Rietveld analysis for the powders of the two extreme size classes showing the contributions of the two Al phases. In large particles, the Al-rich phase predominates in quantity whilst the contributions are similar in small particles indicating a varied amount of trapped solute as a function of cooling rate.

The Al lattice parameter of the average Al phase was calculated with the $\cos\theta\cot\theta$ method. The supersaturated Cu amount is obtained for each particle size fraction by means of the following equation^[45]:

$$a_{Al} = 4.04949 - 0.00483 \cdot \chi_{Cu} \quad [14]$$

where a_{Al} is the measured lattice parameter of the fcc phase and χ_{Cu} is the Copper content expressed as atomic percentage. The Al lattice parameter and the corresponding Cu content are reported in Figure 5. The reference value in Figure 5 is obtained after annealing a representative amount of powder at 803 K for one hour and by cooling in a closed oven overnight approaching as much as possible the equilibrium state. The a_{Al} is lower for particles up to $45 \mu\text{m}$ indicating they have a higher amount of Cu solute in the Al matrix with respect to larger powders where the Cu content appears on average constant. Although it does not vary considerably, it results larger than the maximum solubility given by the equilibrium phase diagram. This quantity ranges from 1.6 to 1.1 wt pct in particles of different size.

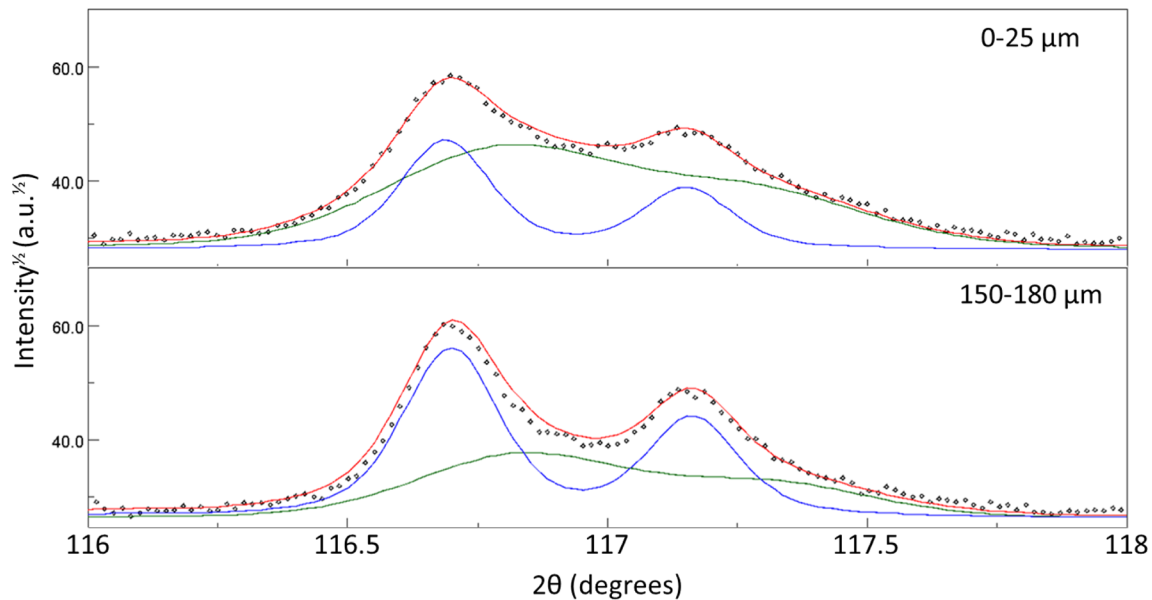


Fig. 4—Example of Rietveld refinement on the (420) peak for particle size classes of $< 25 \mu\text{m}$ and $150\text{-}180 \mu\text{m}$, respectively. The red line refers to the overall refinement whilst the blue line refers to the Al phase being poor in Cu and the green one to the Al phase rich in solute Cu (Color figure online).

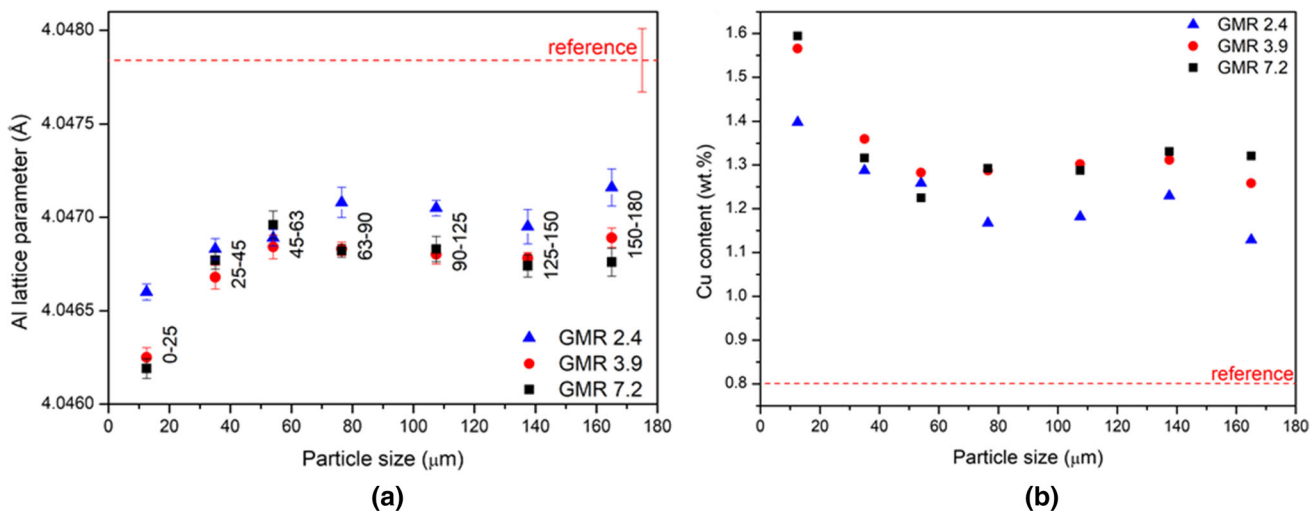


Fig. 5—(a) Al lattice parameter calculated with the $\cos\theta\cot\theta$ method and (b) Cu content in the Al matrix as a function of particle size.

A dependence of the lattice parameter on GMR is evidenced, contrary to the data on particle size (Figure 2(a)). Apparently, the larger amount of gas interacting with fine particles caused faster cooling. Since this was not observed in terms of microstructural features, the more effective heat extraction must have occurred when the powders were already solid. Residual heat and recalescence would have caused Cu precipitation from the primary phase after solidification.

V. CONCLUSIONS

Gas atomization was employed to produce Al-4.5Cu powders. The cell spacing derived from the powder microstructure is the key for the experimental

determination of the correlation existing between the cooling rate and the particles size. The correlation was confirmed by a semi-empirical model which can transfer the knowledge derived from atomization experiments performed on different alloys. The process was discussed utilizing a heat transfer model which also predicts the cooling velocity in gas atomization. The physical variable governing the cooling rate was proven to be the convective heat transfer coefficient and the ratio between inertial forces and viscosity during droplet solidification, which is expressed by the Reynolds number. The model can be useful when coupled with the semi-empirical model in predicting the CR as a function of the particle size for in principle any alloy before running the relative experiment.

From the results of the microstructure analysis, no dependence of the cooling rate during solidification on the GMR can be detected. A combination of XRD and DSC analyses showed that a different fraction of Cu is supersaturated in the Al primary phase depending on droplet solidification rate. The average Cu content varies with particle size and GMR. If the latter increases, the higher the Cu supersaturation. Combining these findings, it is concluded that GMR affects the cooling in the solid-state after solidification causing retention of solute supersaturation in small particles whereas precipitation occurs in larger ones.

ACKNOWLEDGMENTS

Dario Gianoglio acknowledges the STAMP (“Sviluppo Tecnologico dell’Additive Manufacturing in Piemonte”) project for the financial support of his PhD.

FUNDING

Open access funding provided by Università degli Studi di Torino within the CRUI-CARE Agreement.

OPEN ACCESS

This article is licensed under a Creative Commons Attribution 4.0 International License, which permits use, sharing, adaptation, distribution and reproduction in any medium or format, as long as you give appropriate credit to the original author(s) and the source, provide a link to the Creative Commons licence, and indicate if changes were made. The images or other third party material in this article are included in the article’s Creative Commons licence, unless indicated otherwise in a credit line to the material. If material is not included in the article’s Creative Commons licence and your intended use is not permitted by statutory regulation or exceeds the permitted use, you will need to obtain permission directly from the copyright holder. To view a copy of this licence, visit <http://creativecommons.org/licenses/by/4.0/>.

APPENDIX

See Table A1.

Table A1. Process Parameters From the Atomization Experiments and the Resulting GMR Values

	Atomization Run		
	248	248	248
Gas Flow Rate [m ³ /h]	248	248	248
Gas Mass Flow Rate [kg/h]	384,48	384,48	384,48
Melt Mass Flow Rate [kg/h]	158,50	99,70	53,69
GMR	2,43	3,86	7,16

REFERENCES

1. A.M. Mullis, L. Farrell, R.F. Cochrane, and N.J. Adkins: *Metall. Mater. Trans. B*, 2013, vol. 44B, pp. 992–999.
2. G. Kasperovich, T. Volkman, L. Ratke, and D. Herlach: *Metall. Mater. Trans. A*, 2008, vol. 39A, pp. 1183–91.
3. D. Dubè, R. Angers, and A. Adnot: *Pow. Met. Int.*, 1991, vol. 23, pp. 22–25.
4. T.E. Quedest and A.L. Greer: *Acta Mater.*, 2005, vol. 53, pp. 4643–53.
5. M. Paliwal and I.H. Jung: *Acta Mater.*, 2013, vol. 61, pp. 4848–60.
6. W.R. Osório and A. Garcia: *Mater. Sci. Eng. A*, 2002, vol. 325, pp. 103–11.
7. L. Nastac: *Acta Mater.*, 1999, vol. 47, pp. 4253–62.
8. G. Durrant, M. Gallerneault, and B. Cantor: *Mater. Sci. Forum*, 1997, vol. 242, pp. 77–82.
9. D. Tourret and C.A. Gandin: *Acta Mater.*, 2009, vol. 57, pp. 2066–79.
10. D. Shin, A. Shyam, S. Lee, Y. Yamamoto, and J.A. Haynes: *Acta Mater.*, 2017, vol. 141, pp. 327–40.
11. N. Zeoli and S. Gu: *Comput. Mater. Sci.*, 2008, vol. 43, pp. 268–78.
12. G.P. de León, V.E. Lamberti, R.D. Seals, T.M. Abu-Lebdeh, and S.A. Hamoush: *Am. J. Eng. Appl. Sci.*, 2016, vol. 9, pp. 303–22.
13. N. Ciftci, N. Ellendt, G. Coulthard, E. Soares Barreto, L. Mädler, and V. Uhlenwinkel: *Metall. Mater. Trans. B*, 2019, vol. 50, pp. 666–77.
14. J.L. Murray: *Int. Met. Rev.*, 1985, vol. 30, pp. 211–234.
15. O. Zobac, A. Kroupa, A. Zemanova, and K.W. Richter: *Metall. Mater. Trans. A*, 2019, vol. 50A, pp. 3805–15.
16. N. Ponweiser, C.L. Lengauer, and K.W. Richter: *Intermetallics*, 2011, vol. 19, pp. 1737–46.
17. A.C. Reddy: *Int. J. Eng. Sci. Res. Technol.*, 2015, vol. 4, pp. 688–93.
18. W.R. Osório, J.E. Spinelli, I.L. Ferreira, and A. Garcia: *Electrochim. Acta*, 2007, vol. 52, pp. 3265–73.
19. J.M.V. Quaresma, A. Carlos, and A. Garcia: *Metall. Mater. Trans. A*, 2000, vol. 31A, pp. 3167–78.
20. S. Kou: *Welding Metallurgy*, 2nd ed., Wiley, Hoboken, New Jersey, 2003.
21. D. Eskin, Q. Du, D. Ruvalcaba, and L. Katgerman: *Mater. Sci. Eng. A*, 2005, vol. 405, pp. 1–10.
22. W. Kurz and R. Trivedi: *Mater. Sci. Eng. A*, 1994, vols. 179–180, pp. 46–51.
23. C.G. Levi and R. Mehrabian: *Metall. Trans. A*, 1984, vol. 13, pp. 13–23.
24. J.A. Sarreal and G.J. Abbaschian: *Metall. Trans. A*, 1986, vol. 17, pp. 2063–73.
25. T. Liu, J.D. Leazer, S.K. Menon, and L.N. Brewer: *Surf. Coatings Technol.*, 2018, vol. 350, pp. 621–32.
26. A. Prasad, H. Henein, E. Maire, and C.A. Gandin: *Metall. Mater. Trans. A Phys. Metall. Mater. Sci.*, 2006, vol. 37, pp. 249–57.
27. Y. Yang, B. Song, Z. Yang, J. Cheng, G. Song, and L. Li: *Metall. Res. Technol.*, 2018, vol. 115, art. no. 506. <https://doi.org/10.1051/metal/2018025>.
28. M. Bedel, G. Reinhart, A.A. Bogno, C.A. Gandin, S. Jacomet, E. Boller, H. Nguyen-Thi, and H. Henein: *Acta Mater.*, 2015, vol. 89, pp. 234–46.
29. J. Valloton, S. Gawor, and H. Henein: *Comput. Mater. Sci.*, 2018, vol. 144, pp. 176–80.
30. J.P. Hirth: *Metall. Trans. A*, 1978, vol. 9, pp. 401–404.
31. Q. Yang, Y.T. Liu, J. Liu, L. Wang, Z. Chen, M.L. Wang, S.Y. Zhong, Y. Wu, and H.W. Wang: *Mater. Des.*, 2019, vol. 182, pp. 1–12.
32. A. Prasad, H. Henein, E. Maire, and C.A. Gandin: *Can. Metall. Q.*, 2004, vol. 43, pp. 273–82.
33. D. Boucharde and J.S. Kirkaldy: *Metall. Mater. Trans. B*, 1997, vol. 28, pp. 651–63.
34. D. Schwenck, N. Ellendt, J. Fischer-Bühner, P. Hofmann, and V. Uhlenwinkel: *Powder Metall.*, 2017, vol. 60, pp. 198–207.
35. E. Vandersluis and C. Ravindran: *Metallogr. Microstruct. Anal.*, 2017, vol. 6, pp. 89–94.
36. L. Lutterotti, S. Matthies, and H.R. Wenk: *IUCr Newsl. CPD*, 1999, vol. 21, pp. 14–15.
37. W. Ranz: *Chem. Engn. Prog.*, 1952, vol. 48, pp. 173–80.

38. J.B. Wiskel, K. Navel, H. Henein, and E. Maire: *Can. Metall. Q.*, 2002, vol. 41, pp. 193–204.
39. N.J. Grant: *J. Met.*, 1983, vol. 35, pp. 20–27.
40. P.S. Grant, B. Cantor, and L. Katgerman: *Acta Metall. Mater.*, 1993, vol. 41, pp. 3097–3108.
41. A. Plotkowski, K. Fezi, and M.J.M. Krane: *TMS Annu. Meet.*, 2015, vol. 2015-March, pp. 65–72.
42. *Thermo-Calc Software*, TCS AI-based Alloy Database Version 2020b.
43. T.W. Clyne: *Metall. Trans. B*, 1984, vol. 15, pp. 369–81.
44. M. Fatmi, B. Ghebouli, M.A. Ghebouli, T. Chihi, E.H. Ouakdi, and Z.A. Heiba: *Chin. J. Phys.*, 2013, vol. 51, pp. 1019–32.
45. W.B. Pearson: *A Handbook of Lattice Spacings and Structures of Metals and Alloys*, Pergamon Press Ltd., London, 1967.

Publisher's Note Springer Nature remains neutral with regard to jurisdictional claims in published maps and institutional affiliations.